Geophysical Journal International

Geophys. J. Int. (2021) **226,** 803–813
Advance Access publication 2021 April 12
GJI Seismology

doi: 10.1093/gji/ggab136

Multitechnology characterization of an unusual surface rupturing intraplate earthquake: the M_L 5.4 2019 Le Teil event in France

A. Vallage [1], L. Bollinger,[1] J. Champenois,[1] C. Duverger,[1] A. Guilhem Trilla [1], B. Hernandez,[1] A. Le Pichon,[1] C. Listowski,[1] G. Mazet-Roux,[1] M. Menager,[1,2] B. Pinel-Puysségur[1] and J. Vergoz[1]

[1] *CEA, DAM, DIF, F-*91297 *Arpajon, France. E-mail: amaury.vallage@cea.fr*
[2] *Université Côte d'Azur, IRD, CNRS, Observatoire de la Côte d'Azur, Géoazur,* 250 *rue Albert Einstein,* 06560 *Valbonne, France*

Received 2021 February 12; in original form 2020 October 13

SUMMARY

Metropolitan France is a region of slow tectonic deformation with sparse seismicity. On 11 November 2019, the M_L 5.4 Le Teil earthquake became the largest seismic event recorded in the last 16 yr. This event was recorded by the national seismic networks and also by a wide variety of other geophysical techniques including infrasound and InSAR measurements. These complementary technologies offer the opportunity to investigate in detail the earthquake source characteristics and the associated ground motion attenuation. Both seismic waveform inversions and InSAR interferogram reveal a shallow rupture on a reverse fault with an associated moment magnitude of 4.8–4.9. Infrasound signals also provide fast evidences pointing towards the area of ground surface displacements, which coincides with La Rouvière fault, in the Cévennes fault system, known as a formerly active normal fault during the Oligocene. The very significant amount of seismic records also helps towards validating the GMPE laws available for the region. This multitechnology characterization documents the kinematics of this rare example of shallow intraplate fault reactivation.

Key words: Satellite geodesy; Earthquake ground motions; Earthquake source observations.

1 INTRODUCTION

The rate of damaging earthquakes in Slowly Deforming Continental Regions (SDCR) is low (e.g. Fenton *et al.* 2006; Camelbeeck *et al.* 2007; Mazzotti 2007; Calais *et al.* 2016). However, these rare events locally expose the population and industries at close distance from seismogenic sources to strong ground motion (e.g. England & Jackson 2011; Liu & Stein 2016). The assessment of the seismic hazard requires precise estimates of the depth of the seismic sources and quantifications of the strong ground motion at the vicinity of the faults, two parameters rarely well resolved (e.g. Atkinson 2015).

Resolving those unknowns is crucial and could benefit from multitechnological approaches involving a combination of seismological, geodetical and infrasound measurements. Indeed, previous studies (e.g. Le Pichon *et al.* 2003, Pilger *et al.* 2019) demonstrated that the combination of these geophysical techniques was particularly efficient at capturing the complexity of seismological sources for some of the largest earthquakes (Kunlun 2001, Sumatra 2006, Tohoku-Oki 2011 and Sulawesi 2018).

Metropolitan France is a typical SDCR affected by strain rates around 1–2 $\times$ 10^{-9} yr^{-1} (Masson *et al.* 2019; Mazzotti *et al.* 2020) where fault slip-rates remain associated with large uncertainties (e.g. Jomard *et al.* 2017; Vallage & Bollinger 2020) and low to moderate seismicity rates (Cara *et al.* 2015; Manchuel *et al.* 2018).

On 11 November 2019, at 10:52 UTC an earthquake with a local magnitude (M_L) 5.4 occurred in close vicinity of Le Teil which was severely damaged (epicentral intensity VII to VIII EMS98) by the main shock (Figs 1 and 2). Despite its moderate size, this seismic event is the largest earthquake recorded in metropolitan France in the past 16 yr; the last larger event (M_L 5.4, M_w 4.9) occurred in Rambervillers on the 22 February 2003 (Sèbe *et al.* 2018).

In this paper, we investigate the earthquake source using three different, yet complementary, technologies: seismic, InSAR interferometry and infrasound.

2 SEISMOTECTONIC CONTEXT

The M_L 5.4 earthquake was recorded and analysed by the CEA/LDG (Laboratoire de Détection et de Géophysique), which is in charge of rapidly locating M3.5 + earthquakes in the metropolitan territory and informing the national authorities, and also operates as the French national data centre in the frame of the CTBTO (Comprehensive nuclear-test-ban treaty organization). Local and regional data helped locate the event (Fig. 1). An automatic location (44.52°N, 4.74°E) at the origin time 10:52:45.3 UTC and a magnitude M_L of

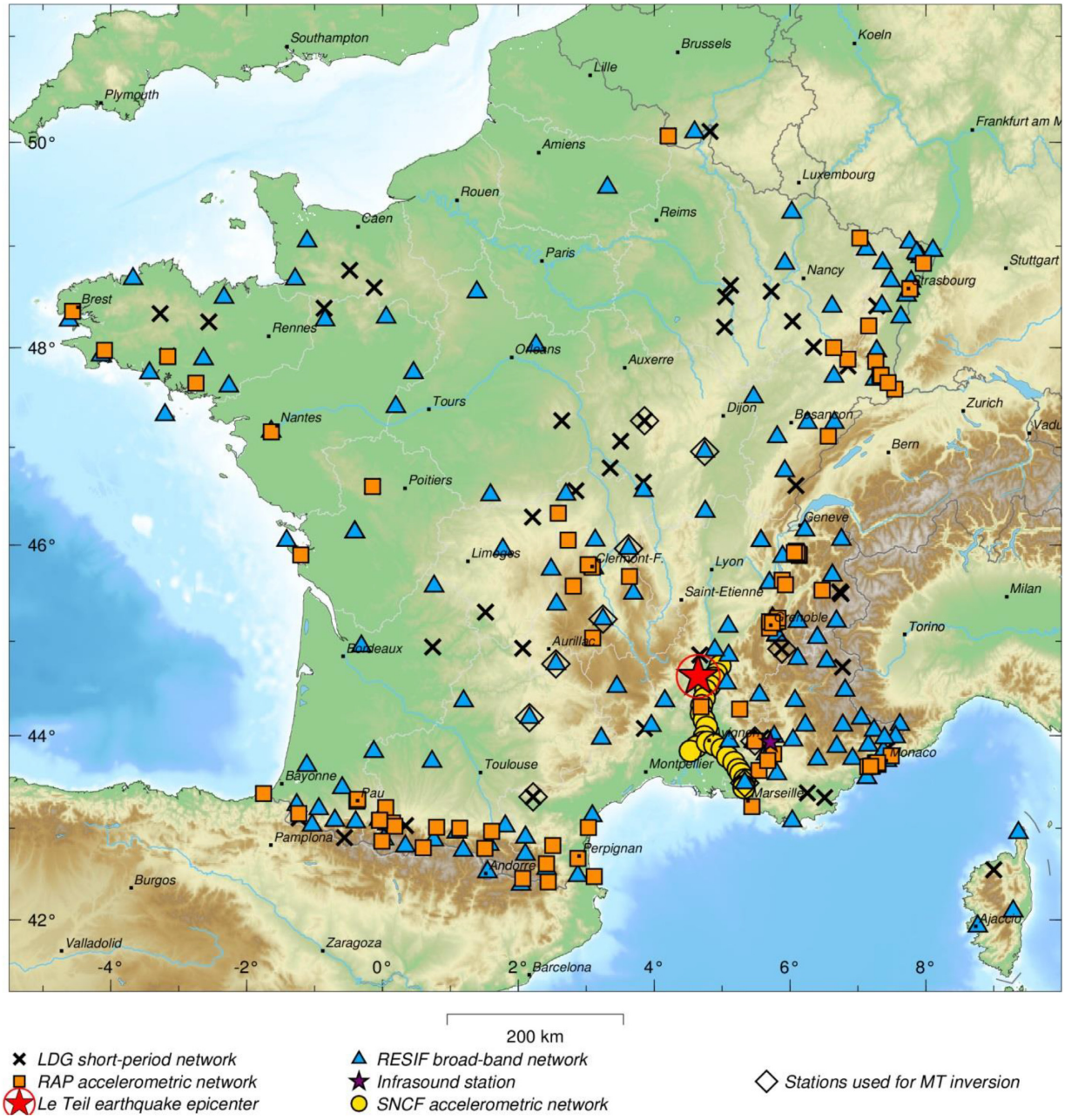

Figure 1. Geophysical networks in France used to characterize the M_L 5.4 Le Teil earthquake.

5.4 calculated from the records of 34 stations were published 12 min after its occurrence time. Later, a manually revised solution using 145 regional stations (306 *P*- and *S*-wave picks) from CEA, RESIF and foreign networks, locates the event ∼8 km westward to its automatic position (44.54°N, 4.65°E, at the origin time 10:52:46 UTC), near the town of Le Teil (Fig. 2). The location of the main shock falls in the vicinity of the Rouvière fault, a ∼5-km-long fault segment that belongs to the Cévennes fault system.

In the epicentral area, upper Cretaceous formations of the Ardèche palaeomargin, mostly composed of marls and shales, are from time to time intercalated with limestone horizons, forming the strongest elements of the local relief (Elmi *et al.* 1996; Fig. 2). These rocks are affected by a 10-km-wide fault-and-fold system trending NE–SW, which runs between the Cévennes and Marsanne faults (Fig. 2, e.g. Jomard *et al.* 2017).

The geology at depth can be extrapolated from the rock bedding and from fault azimuths and dips reported on local geological maps, and complemented by observations from a 4489 m deep borehole drilled at Valvignères in 1963 by the SNPA (Société Nationale des Pétroles d'Aquitaine, VAL1 on Fig. 2, http://infoterre.brgm.fr). The borehole was drilled down to the basement. It mostly exposed a 400-m-thick Triassic formation overlaid by a 4-km-thick series of Mesozoic rocks (mainly marls and clays). These marls and clays successions sandwich a 150-m-thick rigid Tithonian recifal limestone (i.e. made of Kimmeridgian to Berriasian limestones) reached between –766 and –927 m in the borehole.

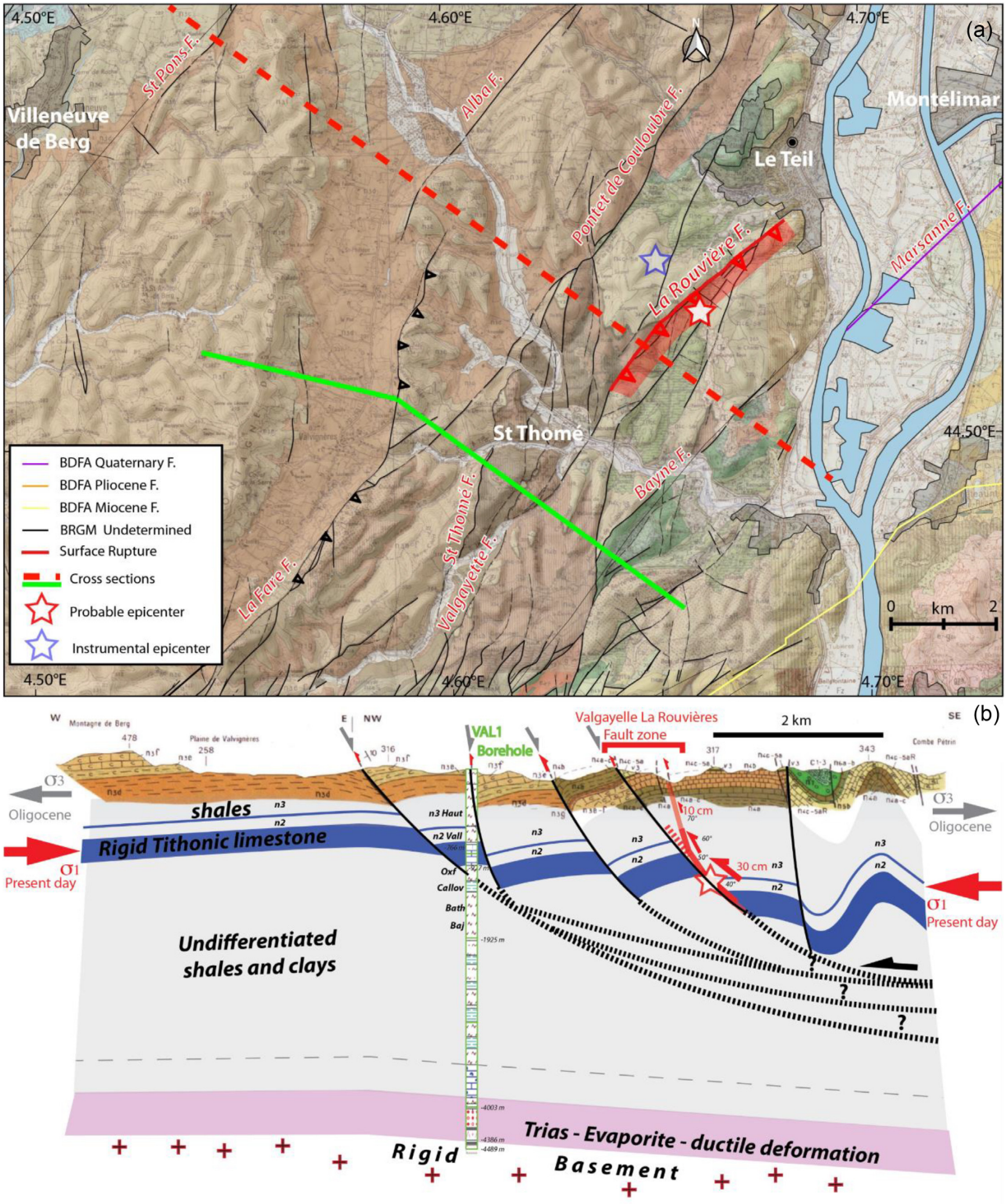

Figure 2. (a) Local geological setting showing the regional faults and the different Le Teil epicentres discussed here. (b) Cross-section view of the fault zone responsible for the M_L 5.4 Le Teil earthquake. See Fig. S1 for more information regarding the cross-section.

The surface mapped faults dip rather steeply (40–80°) to the southeast. They expose a cumulative normal offset of several hundreds of metres, mostly attributed to an extensional phase during the Oligocene West-European rifting (Bergerat 1987). The structural style of the fault system is similar to what was observed southward, along the Ardèche boundary cross-section documented in the Deep Geology of France (DGF) program by seismic lines, scientific boreholes and balanced cross sections, which described curved or listric normal faults (Bonijoly *et al.* 1996). These normal faults progressively flatten at depth, probably rooting on a decollement level within the marls and clays of the Jurassic, by analogy to what has been documented southward along the Ardèche transect of the DGF (Fig. 2).

3 SOURCE CHARACTERISTICS

The source characteristics are investigated using three different, yet complementary, technologies: seismic, InSAR interferometry and infrasound.

3.1 Seismological characterization

The focal mechanism of the main shock is determined using time-domain deviatoric moment tensor inversions (TDMT_INVC, Dreger 2003, see Text S1) based on 10 three-component CEA and RESIF seismic stations, up to 310 km from the revised epicentre (Figs 1 and 3). Velocity records are deconvolved with instrument responses, integrated to displacement and then filtered between 12.5 and 33 s period. This frequency band constitutes the best compromise permitting a point-source approximation for the waveform inversion at all the selected stations. To constrain the source parameters, inversions are calculated between 0.5 and 20 km depth using a point source assumption at the revised epicentre and the LDG 1-D velocity model composed of three layers and used at the LDG for routine earthquake locations in France since 1975 (Fig. S2). Fig. 3(b) reveals that a very shallow (∼0.5–2 km depth) source is well defined, with a confidence level reaching 83 per cent of variance reduction (VR, 100 per cent meaning a perfect fit between observed data and synthetics). Given the similar waveform fits between 0.5 and 2 km depth (Fig. 3b) the solution at 1 km depth is preferred to describe the seismic source based on its highest double-couple component. Fig. 3(a) shows the event's reverse focal mechanism. Its strike (N47°) and dip (65°) agree with the Rouvière fault characteristics. Strike and dip directions are given following the Aki & Richards (2002) convention. This M_w 4.8 reverse source is confirmed when performing a Jackknife statistical test (Fig. S3 and Table S1) and when using a moment tensor grid search approach and the same 10 stations (Fig. S4). Furthermore, the best solution of the grid search locates the event on the fault zone (Fig. 2).

In addition, teleseismic data from 48 well-distributed broad-band stations are used to estimate the 20-s period surface wave magnitude (M_s) of 4.2 ± 0.3 following the approach defined by Vanek *et al.* (1962). This M_s value is in agreement with the M_s value published by the International Data Centre of the Comprehensive Nuclear-Test-Ban Treaty Organization (CTBTO), and with more complex MSVMAX measurements (Bonner *et al.* 2006). See Text S1 and Fig. S5 for details regarding the M_s calculation.

Finally, the Le Teil hypocentre lies at (or immediately below) the bottom limit of the top layer of the LDG velocity model (i.e. 0.9 km, Fig. S2). Given the characteristics of the two crustal layers, an average shear wave velocity (Vs) of ∼2.8 km s^{-1} can be estimated for the rupture plane for a bulk density of 2700 kg m^{-3}. These values are consistent with velocities and densities of limestones (e.g. Carmichael 1984). A resulting mean shear modulus of ∼21.1 GPa will be used to compare the seismological and geodetical solutions for the sake of consistency.

3.2 InSAR characterization

Sentinel-1 C-band SAR images from four tracks (two descending and two ascending) are used (https://scihub.copernicus.eu/) to produce coseismic interferograms (Table S1). All interferograms are processed with the SNAP software (https://step.esa.int/main/toolboxes/snap/). Based on this conventional Differential SAR Interferometry (DInSAR), a significant phase signal of surface displacement is observed in the vicinity of the M_L 5.4 Le Teil 2019 earthquake (Figs 4b and S7). The selected interferograms are not affected by significant atmospheric effects. A clear phase discontinuity can be followed over ∼5 km suggesting that the rupture reached the surface. The trend of the derived rupture trace shows an azimuth of N45°.

This InSAR data set, including ascending and descending tracks and different incidence angles, is used to invert InSAR surface displacements following Barnhart & Lohman (2010) and Barnhart *et al.* (2014). The geodetic inversion is performed in order to help constrain the dip, rake and slip distribution along the fault plane. The strike value is fixed at N45° as stated by the main surface rupture trace while fault width and length are respectively fixed at 4 and 7 km. The InSAR data inversion is tested with dip angle values ranging from 30° to 80° every 10°. The best fitting model is obtained with a dip angle of 60° and a mean rake angle value of 108°. The mean rake angle remains around 108° whatever the dip angle used in the inversion. Fig. 4a shows that the corresponding focal mechanism is in very good agreement with the solution of the seismic moment tensor inversion.

The slip distribution (Fig. 4c) extracted from 'best-fitting model' (Figs S8 and S9) matches well the InSAR observation with RMS misfits ranging between 0.28 and 0.48 cm. The residuals between InSAR data and predicted displacements are larger close to the surface rupture mainly due to our choice of a simplified linear fault geometry in the slip inversion. The slip distribution derived from our best fitting model shows that most of the slip occurred at 1 km depth with a maximum slip value of 27 cm. Rake angle values indicate a nearly perfect reverse slip at depth and a reverse plus right lateral slip at surface.

Along strike, close to the surface, slip values range between 2 and 25 cm (Fig. 4c) in good agreement with measurements made in the field (Ritz *et al.* 2020). If adopting the same seismological shear modulus value of 21.1 GPa, the equivalent earthquake moment magnitude M_w is 4.9.

3.3 Infrasound characterization

The sudden ground motion in the epicentral area was large enough to generate infrasound signals that were detected by a four-element infrasound array, of 1 km aperture, installed at the Haute-Provence Observatory (OHP). Due to the shallow depth of the earthquake and the fact that the earthquake ruptured the surface, part of the infrasound could originate from the seismic energy evanescently coupling phenomena as shown by Evers *et al.* (2014). Located at a distance of 107 km in the geometrical shadow zone, this station recorded signals of amplitude 0.035 Pa (zero-to-peak) at a dominant frequency of 1 Hz.

When adding wind perturbations induced by naturally occurring gravity waves, which are not fully resolved by the European Centre for Medium-Range Weather Forecasts (ECMWF), Integrated Forecast System (IFS) atmospheric specifications (cycle 38r2), parabolic equation and normal mode propagation simulations (Text S4) predict at OHP partial reflections from stratospheric altitudes at about 30 km. Considering realistic wind perturbations (Fig. S11 and Text S4) as measured by lidar sounding (Le Pichon *et al.* 2015), the transmission loss (attenuation) is estimated to be 70 ± 5 dB with respect to a reference distance of 1 km from the source.

The geographical source locations of the ground-to-air coupling regions and peak surface pressure (PSP) are calculated from the measured arrival times, backazimuth and signal amplitude at OHP by applying the inverse location procedure described by Hernandez

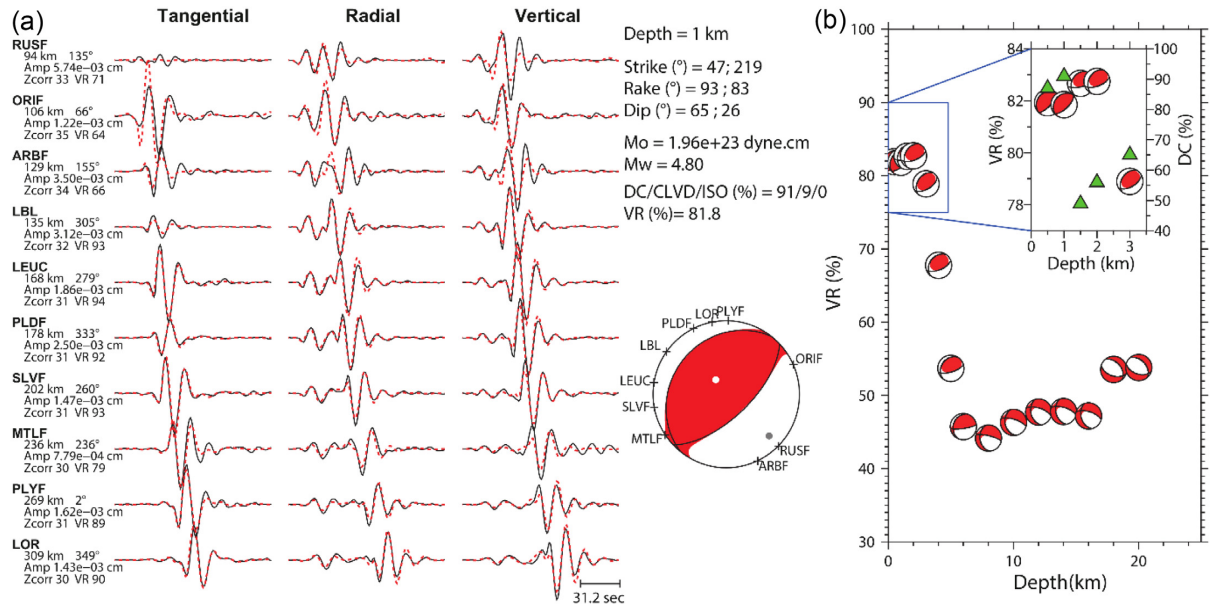

Figure 3. Moment tensor solutions using 10 regional CEA and RESIF seismic stations between 95 and 310 km from the revised epicentre. (a) Waveform comparison between observed data (black) and synthetics (dashed red line) for the preferred solution at 1 km depth. (b) Depth effect on the variance reductions (VR) of the moment tensor solutions between 0.5 and 20 km depth. The inset shows the solutions between 0.5 and 3 km depth both in terms of VR (by the beachball mechanisms) and double-couple (DC) components (green triangles). The best solutions are found between 0.5 and 2 km depth.

et al. (2018) and recalled in text S3. This leads to the mapping of the coupling region shown in Fig. 4(d). Back-projecting the infrasound measurements at OHP using the predicted attenuation and assuming a geometrical spreading of the pressure wave radiating from the reference distance of 1 km surface to the observation distance R_0, sound pressure level (SPL) values of 120 ± 5 dB are inferred (Fig. 4d). PSP (in Pa) is related to SPL (dB) via the following relationship: $\mathrm{SPL} = 20\log(\mathrm{PSP}/2\times10^{-5})$. The resulting PSP values 20 Pa here.

4 GROUND MOTION PROPAGATION

The Le Teil earthquake provides the opportunity to measure relative strong ground motions over large distances in such intraplate domain. Data from multiple networks across the country were collected: back-projected infrasound measurement made at the OHP, the French permanent broad-band network (RESIF-RLBP) composed of three-component velocimeters, the French permanent strong motion network (RESIF-RAP) composed of three-component accelerometers, some three-component accelerometers installed along the southeast Mediterranean railway by the French National Railway Company (SNCF) and the CEA/LDG network composed of a combination of three-component and vertical-component velocimeters (Duverger *et al.* 2021). Peak ground accelerations (PGA) are measured on a total of 307 stations of these networks. A total of 850 seismological records and one back-projected infrasound measurement made for the event is noteworthy for a single metropolitan France earthquake. Moreover, the distance range of the measurements (Fig. 5), from 5 to 1000 km, gives us the unseen opportunity to work on near-field moderate-to-strong motion in France and to compare observations with attenuation laws over a large distance range. Causse *et al.* (2021) also proposed to compare quantitative ground accelerations estimated from *in situ* observations of displaced objects and numerical predictions, within a radius of a few kilometres around the Rouvière fault source.

Before extracting PGA on every available record, velocimetric data are converted into accelerations. PGA values are plotted in Fig. 5 as a function of epicentral distances to Le Teil earthquake. Different attenuation curves based on several attenuation laws adapted for the French context are estimated using the magnitudes of Le Teil earthquake (i.e. M_S, M_L and M_w inverted values) and its hypocentre location fixed at 1 km depth. Site condition is fixed at standard rock and source parameters (style of faulting, etc.) are taken into account when needed to express the Ground Motion Prediction Equations (GMPEs) formula. Those correspond to the laws established by Berge-Thierry *et al.* (2003) named BT03 in the following, Marin *et al.* (2004) or Ma04, Drouet & Cotton (2015) or DC15, and Ameri *et al.* (2017) or Am17. Parameters and description of these four GMPEs are further detailed in the Text S7.

Fig. 5 shows that BT03 and Ma04 overvalue most of the records. The two other GMPEs seem coherent with observations at least for their magnitude- and distance-range domains suggested by their authors (Table S3). The behaviour of the DC15 curve clearly differs from others with a much stronger attenuation beyond 200 km even if such pattern appears outside its domain of validity. We can also point that DC15 and Am17 laws predict lower PGA at short distance (<10 km) than BT03 and Ma04 do, which seems in agreement with back-projected infrasound measurement made at the OHP. We computed H/V ratios at PGA for all three-component stations and the average value is very close to the 3/2 factor (Text S7 and Fig. S13), which is a common constant coefficient and most simple approximation applied when no horizontal data are available (RFS 2001-01) for engineering purpose.

5 DISCUSSION ON THE MULTITECHNOLOGY COHERENCY

The different technologies considered here provide valuable results that help better constrain the source characteristics of this event of

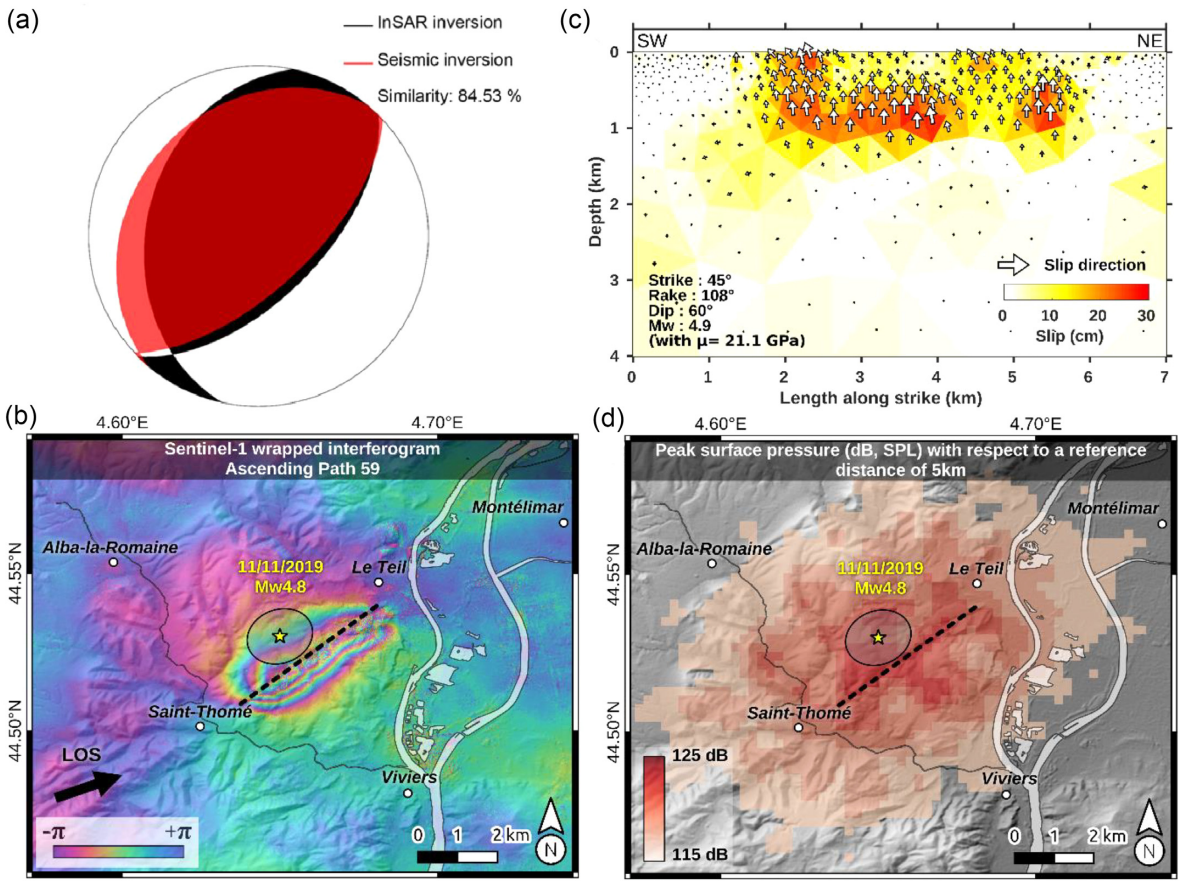

Figure 4. (a) Comparison of the focal mechanisms obtained using seismic inversion (red) and InSAR inversion (black). (b) Wrapped Sentinel-1 interferogram from ascending path 59 between 06 November 2019 and 12 November 2019. Black dashed line represents the inverted fault surface trace. (c) Slip distribution on the fault. The arrows show slip directions of the eastern side of the fault. The earthquake parameters are shown in the lower left-hand corner. (d) Infrasound peak surface pressure (PSP). The signal amplitude is corrected for geometrical spreading and dissipation and calculated in bins of 0.5 × 0.5 km^2. The colourbar codes the PSP levels (in dB) converted into sound pressure level (SPL, standard reference pressure of 20 μPa) with respect to a reference distance of 5 km to the ground surface.

interest, as well as highlight features such as ground motion usable for seismic hazard studies.

5.1 Source mechanism

Two independently derived focal mechanisms using (1) seismic data and (2) InSAR data (Fig. 4a) show a similarity nearly reaching 85 per cent following the method of Rivera & Kanamori (2014). This high quality resolution of the source is remarkable given the parameters considered in both inversions: different data type, frequency band, earth model, type of inversion (i.e. double-couple and deviatoric), etc.

It has to be noted that the InSAR inversion provides a larger slip and seismic moment release at depth. Even though the event magnitude difference between the two data solutions is rather small (i.e. M_w 4.9 versus 4.8), the moment release difference between the two results is of 8.23E + 15 Nm (i.e. M_w 4.54). The slight discrepancies in the source parameters (M_w, strike, dip, rake) inverted from the InSAR and seismic data remain mostly within uncertainties of each method (See Text S1 for a discussion regarding the uncertainties in the moment tensor solution).

Such differences could be explained by local geological effects and methodology uncertainties. In addition, seismic data and InSAR data are not sensitive to the same parameters. InSAR data images the ground displacement at the surface within the line of sights of the satellite. The slip inversion at depth on the fault plane does incorporate a displacement integrated over a few days (Table S2). The dip value of 60° towards the SE could be consistent with the average dip value of the listric fault, from 70° within the first hundreds of metres to ∼40° at the hypocentral depth (Fig. 2). The seismic inversion, on the other hand, makes assumption of a temporal and spatial point source given the inverted wavelength and the simple earth model considered, without imposing the fault strike. However, the rupture of Le Teil main shock lasted ∼35 s over a finite fault and triggered a strong vibration of the Tithonian recifal limestone (Fig. 2b). One can make the hypothesis that the larger moment release inverted by InSAR resulted from a very shallow, and partly, aseismic slip through the clays and marls in the subsurface.

This study shows that the two approaches bring quality information about the source mechanism, which could be lost when performing a joint inversion.

5.2 Multitechnology ground motion comparison

The PSP spatial distribution (Fig. 4d) inferred from infrasound observations can be compared to the surface displacement calculated from InSAR (Fig. S10b). It is noteworthy that regions with the maximum PSP coincide with the fault orientation where the maximum

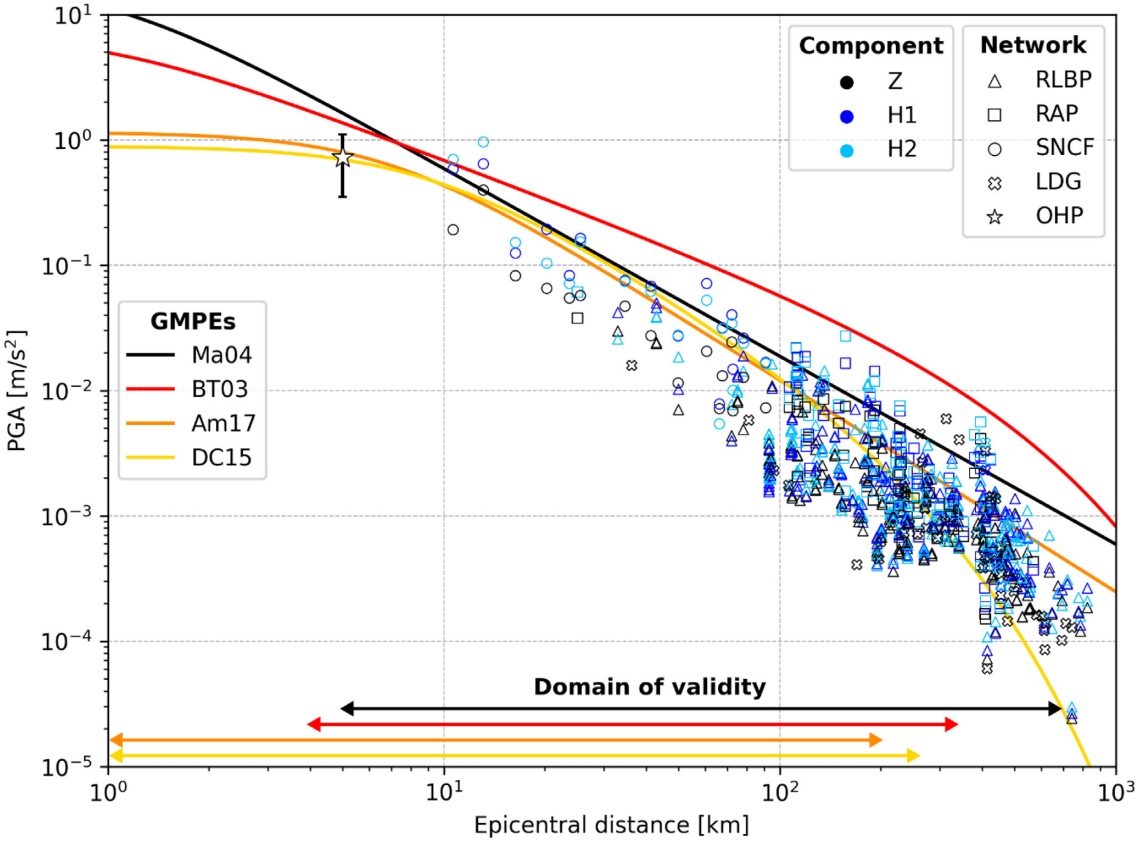

Figure 5. PGA values (in m s^{-2}) as a function of epicentral distance (in km). Measures on vertical component are represented in black whereas measures on the two horizontal components are in light and dark blue, respectively. PGAs are estimated over the RLBP (triangle), the RAP (square), the LDG (crosses) the OHP (star) and the SNCF (circle) seismic stations. The four Ground Motion Prediction Equations discussed in the paper are superimposed on the data with their distance-range domain of validity indicated by coloured arrows.

surface displacement occurred (Figs S10a and S10b). The displacement inverted from InSAR has been resampled to the PSP map, which is less resolved, giving 961 measurement points. The offset between the barycentre of the two measurement maps is less than 2 km. After compensating this offset, the Spearman correlation coefficient (Spearman 1904) between these two quantities values 0.79 (Text S6). This coefficient does not impose a linear relationship between the quantities. The null hypothesis of independence between the variables can be rejected with a probability greater than 1×10^{-7}, confirming the visually good agreement observed on Figs 4(c) and (d). One can observe a quasi-symmetry in the southwest–northeast direction in both PSP and satellite observations. This symmetry reflects a bilateral source directivity consistent with the effects of the rupture directivity on ground shaking. The maximum PSP covers regions where the surface reached the maximum displacement (∼5–8 cm, Figs S10a and b).

On the other hand, to relate PSP to peak ground acceleration (PGA), the spatial distribution of the measured PGA is discretized into a grid of adjacent source elements (circular pistons) of radius Rp using the procedure described in Walker *et al.* (2013) as explained in text S3. The equation obtained is: PSP(x,y) (Pa) = 31.8 PGA(x,y) (m s^{-2})

where x,y are the coordinates of the considered surface element. In doing so, PSP values at Le Teil, obtained following the method described in Section 2.3, yield a maximum vertical acceleration ranging from 0.35 to 1.1 m s^{-2}. It is noteworthy that PGA estimated from infrasound back-projection falls within range of PGA values extrapolated at an epicentral distance of 5 km (Fig. 5).

These findings, supported by the comparison with empirical amplitude–magnitude scaling relation, indicate that the infrasound amplitude, corrected for propagation effects, is primarily driven by the seismic magnitude (Fig. 6). The deviation observed for the shallow Le Teil and deep M7.3 China earthquakes, suggests that, beyond the seismic magnitude, infrasound may also provide information about focal depth.

6 CONCLUSIONS

The M_L5.4 Le Teil earthquake is unusual in several aspects, starting with the observation of surface ruptures for such a moderate earthquake. It is also the first time that an earthquake occurring in metropolitan France is examined with such amount of state-of-the-art and different technologies. Its location has been revised with a large number of phase picking at local and regional seismic stations. Different types of magnitudes (M_L 5.4, M_S 4.2 ± 0.3 and M_w 4.8–4.9) calculated using regional and teleseismic data are provided. Moreover, its source focal mechanism is highly constrained by seismic data and InSAR measurements separately. Infrasound and InSAR data tend to agree on the event's ground deformation. Altogether, the multiple approaches showed here helps providing an outstanding reading of the main shock despite its moderate magnitude. By investigating the resemblances and the discrepancies in the results one can point out their physical meanings, for example in terms of slip pattern and/or resolution differences.

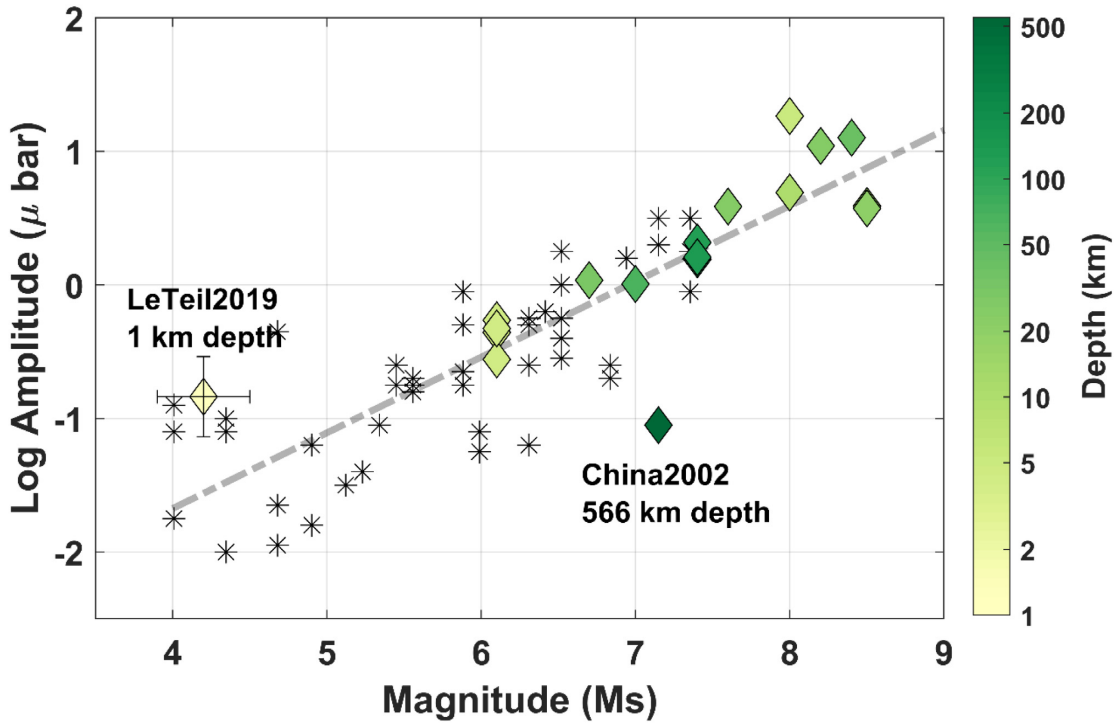

Figure 6. Relation between earthquake surface wave magnitude (M_s) with depth and wind-corrected amplitudes of infrasound signals observed from shallow to deep earthquakes (stars adapted from Mutschlecner & Whitaker 2005; diamonds from Le Pichon *et al.* 2006). The Le Teil event is reported along with its corresponding uncertainties. The linear scaling relation (black dashed line) is the best fit of this dataset: $y = 0.57x - 3.94$. The normalized infrasound amplitude is well correlated to the ground motion strength for a wide range of magnitudes.

Results obtained from seismic and InSAR data illustrate the different processes captured according to the involved technology. Long period seismic data highlight the coseismic rupture of a rigid 0.5–1.5 km deep geological layer on a suspected flattening fault. In contrast the InSAR data captures the integrated deformation over several days and up to the surface, on a shallower and steeper part of the fault in soft geological material.

Furthermore, although the existing infrasound network is not favourable to capture details in the event's radiated pressure waves, analysis of the signals recorded at one single station helps to reconstruct both the geographical coverage and the surface shaking intensities in the epicentral region. Such observation complements the ones obtained by satellite imagery and seismometers. Our results show that this technique provides information on the surface rupture location even for a weak event and faster than the return period of SAR satellites. Considered in addition to seismic data, it would be useful before starting early fieldwork investigations. A PSP threshold above which one could expect surface rupture should also be defined in the future.

The different results obtained from the three technologies used here give complementary, but yet independent, information to evaluate the severity of shaking, even for such a moderate earthquake. The unprecedented amount of ground motion measurements for metropolitan France will also provide key parameters to further work on motion propagation and future attenuation law implementation in seismic hazard assessment models. All the techniques agree on the re-activation as a thrust of a former normal fault, which is often the case in intraplate regions. Such opposite motion reactivation highlights the complexity of modelling faults impact on seismic hazard assessment when only relying on old and inherited sense of deformation in regions of low deformation rates.

ACKNOWLEDGEMENTS

The authors are grateful to Y. Cano, P. Herry and S. Merrer for their early stage work on the different technologies in order to characterize the event. The authors acknowledge the detailed review provided by Christoph Pilger, one anonymous reviewer and the editor Eiichi Fukuyama.

DATA AVAILABILITY STATEMENTS

RESIF is a national Research Infrastructure, recognized as such by the French Ministry of higher education and research. RESIF is managed by the RESIF Consortium, composed of 18 Research institutions and universities in France. RESIF additionally supported by a public grant overseen by the French national research agency (ANR) as part of the 'Investissements d'Avenir' program (reference: ANR-11-EQPX-0040) and the French Ministry of environment, energy and sea (http://dx.doi.org/10.15778/RESIF.FR; http://seismology.resif.fr/#NetworkConsultPlace:FR)

Accelerometric data from the emergency stopping system of the Mediterranean LGV were kindly provided by SNCF. PGA measurements available at: https://data.mendeley.com/datasets/sysz47grjj/1

The facilities of IRIS Data Services, and specifically the IRIS Data Management Centre, were used for access to waveforms, related metadata, and/or derived products used in this study. IRIS Data Services are funded through the Seismological Facilities for the Advancement of Geoscience (SAGE) Award of the National Science Foundation under Cooperative Support Agreement EAR-1 851 048 (http://ds.iris.edu/ds/nodes/dmc/data/sources/)

Contains modified Copernicus Sentinel data 2019 (https://scihub.copernicus.eu/).

REFERENCES

Ameri, G., Drouet, S., Traversa, P., Bindi, D. & Cotton, F., 2017. Toward an empirical ground motion prediction equation for France: accounting for regional differences in the source stress parameter, *Bull. Earthq. Eng.,* **15**(11), 4681–4717.

Aki, K. & Richards, P.G., 2002. *Quantitative Seismology,* 2nd edn, University Science Books, ISBN 0-935702-96-2.

Assink, J.D., Le Pichon, A., Blanc, E., Kallel, M. & Khemiri, L., 2014. Evaluation of wind and temperature profiles from ECMWF analysis on two hemispheres using volcanic infrasound, *J. Geophys. Res. Atmos.,* **119,** doi:10.1002/2014JD021632.

Atkinson, G.M., 2015. Ground-motion prediction equation for small-to-moderate events at short hypocentral distances, with application to induced-seismicity hazards, *Bull. seism. Soc. Am.,* **105**(2A), 981–992.

Barnhart, W.D. & Lohman, R.B., 2010. Automated fault model discretization for inversions for coseismic slip distributions, *J. geophys. Res.,* **115,** B10419, doi:10.1029/2010JB007545.

Barnhart, W.D., Benz, H.M., Hayes, G.P., Rubinstein, J.L. & Bergman, E., 2014. Seismological and geodetic constraints on the 2011 Mw5.3 Trinidad, Colorado earthquake and induced deformation in the Raton basin, *J. geophys. Res.,* **119,** 7923–7933.

Berge-Thierry, C., Cotton, F., Scotti, O., Griot-Pommera, D.A. & Fukushima, Y., 2003. New empirical response spectral attenuation laws for moderate European earthquakes, *J. Earthq. Engineering,* **7**(02), 193–222.

Bergerat, F., 1987. Stress fields in the European platform at the time of Africa-Eurasia collision, *Tectonics,* **6**(2), 99–132.

Bertin, M., Millet, C. & Bouche, D., 2014. A low-order reduced model for the long-range propagation of infrasounds in the atmosphere, *J. acoust. Soc. Am.,* **136**(1), 37–52.

Blixt, M., Näsholm, S.P., Gibbons, S., Evers, L., Charlton-Perez, A., Orsolini, Y. & Kværna, T., 2019. Estimating tropospheric and stratospheric winds using infrasound from explosions, *J. Acoust. Soc. Am.,* **146,** doi:10.1121/1.5120183.

Bonijoly, D., Perrin, J., Roure, F., Bergerat, F., Courel, L., Elmi, S. & Mignot, A., 1996. The Ardeche palaeomargin of the South-East Basin of France: mesozoic evolution of a part of the Tethyan continental margin, Géologie Profonde de la France programme, *Mar. Petrol. Geol.,* **13**(6), 607–623.

Bonner, J.L., Russell, D., Harkrider, D., Reiter, D. & Herrmann, R., 2006. Development of a time-domain, variable-period surface wave magnitude measurement procedure for application at regional and teleseismic distances, Part II: application and Ms —mb performance, *Bull. seism. Soc. Am.,* **96,** 678–696

Calais, E., Camelbeeck., T., Stein, S., Liu, M. & Craig, T.J., 2016. A new paradigm for large earthquakes in stable continental plate interiors, *Geophys. Res. Lett.,* **43,** doi:10.1002/2016GL070815.

Camelbeeck, T. *et al.*, 2007. Relevance of active faulting and seismicity studies to assessments of long-term earthquake activity and maximum magnitude in intraplate northwest Europe, between the Lower Rhine Embayment and the North Sea, *Spec. Pap.-Geol. Soc. Am.,* **425,** 193–224.

Cara, M., Cansi, Y., Schlupp, A., Arroucau, P., Béthoux, N., Beucler, E. & Van Der Woerd, K., 2015. SI-Hex: a new catalogue of instrumental seismicity for metropolitan France, *Bull. Soc. Géol. France,* **186**(1), 3–19.

Carmichael, R.S.(ed.), 1984. *Handbook of Physical Properties of Rocks,* CRC Press.

Causse, M. *et al.*, 2021. Exceptional ground motion during the shallow Mw 4.9 2019 Le Teil earthquake, *France Commun. Earth Environ.,* **2,** 14.

Chen, C.W. & Zebker, H.A., 2001. Two-dimensional phase unwrapping with use of statistical models for cost functions in nonlinear optimization, *J. Opt. Soc. Am., A,* **18**(2), 338–351.

Cugnet, D., De la Cámara, A., Lott, F., Millet, C. & Ribstein, B., 2018, . Non-orographic gravity waves: representation in climate models and effects on infrasound, in *Infrasound Monitoring For Atmospheric Studies,* 2nd edn, pp. 349–386, eds Le Pichon, A., Blanc, E. & Hauchecorne, A., Springer Nature, ISBN: 978-3-319-75140-5.

Damiens, F., Millet, C. & Lott, F., 2018. An investigation of infrasound propagation over mountain ranges, *J. acoust. Soc. Am,* **143,** 563, doi:10.1121/1.5020783.

Dreger, D.S., 2003. TDMT_INV: time domain seismic moment tensor INVersion, *International Handbook of Earthquake and Engineering Seismology,* Vol. **81B,** 1627pp.

Drouet, S. & Cotton, F., 2015. Regional stochastic GMPEs in low-seismicity areas: scaling and aleatory variability analysis—application to the French Alps, *Bull. seism. Soc. Am.,* **105**(4), 1883–1902.

Duverger, C. *et al.*, 2021. A decade of seismicity in metropolitan France (2010-2019): the CEA/LDG methodologies and observations, *BSGF - Earth Sci. Bull.,* 25 March 2021, doi.org/10.1051/bsgf/2021014.

Elmi, S., Busnardo, R., Clavel, B., Camus, G., Kieffer, G., Bérard, P. & Michaëly, B., 1996. Carte géologique de la France au 1/50.000, feuille Aubenas (865. Bureau de Recherches Géologiques et Minières, *Notice explicative,* 170.

England, P. & Jackson, J., 2011. Uncharted seismic risk, *Nat. Geosci.,* **4**(6), 348–349.

Evers, L.G. *et al.*, 2014. Evanescent wave coupling in a geophysical system: airborne acoustic signals from the mw 8.1 Macquarie ridge earthquake, *Geophys. Res. Lett.,* **41,** 1644–1650.

Fenton, C., Adams, J. & Halchuk, S., 2006. Seismic hazards assessment for radioactive waste disposal sites in regions of low seismic activity, *Geotech. Geol. Eng.,* **24,** 579–592.

Fritts, D.C. & Alexander, M.J., 2003. Gravity wave dynamics and effects in the middle atmosphere, *Rev. Geophys.,* **41,** 1003, doi:10.1029/2001RG000106.

Gardner, C.S., Hostetler, C.A. & Franke, S.J., 1993. Gravity wave models for the horizontal wave number spectra of atmospheric velocity and density fluctuations, *J. geophys. Res.,* **98,** 1035–1049.

Green, D.N., Vergoz, J., Gibson, R., Pichon, A.Le & Ceranna, L., 2011. Infrasound radiated by the Gerdec and Chelopechene explosions: propagation along unexpected paths, *Geophys. J. Int.,* **185**(2), 890–910.

Guilhem, A., Cano, Y. & Plantet, J.L., 2015. MSVMAX: implementation and developments of an operational tool for event characterization at the French National Data Center, *CTBTO Science and Technology,* Vienna, Austria.

Guilhem Trilla, A. & Cano, Y., 2017. Constraining the explosive nature of the DPRK nuclear events at regional scale using moment tensor inversions and MSVMAX, *CTBTO Science and Technology,* Vienna, Austria.

Hernandez, B., Le Pichon, A., J.Vergoz, P.H, Ceranna, L., Pilger, C., Marchetti, E., Ripepe, M. & Bossu, R., 2018. Estimating the ground-motion distribution of the 2016 Mw 6.2 Amatrice, Italy earthquake using remote infrasound observations, *Seismol. Res. Lett.,* **89,** doi:10.1785/0220180103.

Jomard, H., Cushing, E.M., Palumbo, L., Baize, S., David, C. & Chartier, T., 2017. Transposing an active fault database into a seismic hazard fault model for nuclear facilities–Part 1: building a database of potentially active faults, BDFA) for metropolitan France, *Nat. Hazards Earth Syst. Sci.,* **17**(9), 1573–1584.

Kendall, M.G., 1938. A new measure of rank correlation, *Biometrika,* **30**(1–2), 81–93.

Kulichkov, S.N., Chunchuzov, I.P. & Pupov, O.I., 2010) Simulating the influence of an atmospheric fine inhomogeneous structure on long-range propagation of pulsed acoustic signals, *Izv. Atmos. Ocean Phys.,* **46**(1), 60–68

Le Pichon, A., Guilbert, J., Vallée, M., Dessa, J.X. & Ulziibat, M., 2003. Infrasonic imaging of the Kulun Mountains for the great 2001 China earthquake, *Geophys. Res. Lett.,* **30,** 1814, doi:10.1029/2003GL017581, 15.

Le Pichon, A., Mialle, P., Guilbert, J. & Vergoz, J., 2006. Multi-station infrasonic observations of the Chilean earthquake of 2005 June 13, *Geophys. J. Int.,* **167,** 838–844.

Le Pichon, A. *et al.*, 2015. Comparison of co-located independent ground-based middle-atmospheric wind and temperature measurements with numerical weather prediction models, *J. Geophys. Res. Atmos.,* **120,** doi:10.1002/2015JD023273.

Liu, M. & Stein, S., 2016. Mid-continental earthquakes: spatiotemporal occurrences, causes, and hazards, *Earth-Sci. Rev.,* **162,** 364–386.

Manchuel, K., Traversa, P., Baumont, D., Cara, M., Nayman, E. & Durouchoux, C., 2018. The French seismic CATalogue, FCAT-17, *Bull. Earthq. Eng.,* **16**(6), 2227–2251.

Marin, S., Avouac, J.P., Nicolas, M. & Schlupp, A., 2004. A probabilistic approach to seismic hazard in metropolitan France, *Bull. seism. Soc. Am.,* **94**(6), 2137–2163.

Masson, C., Mazzotti, S., Vernant, P. & Doerflinger, E., 2019. Extracting small deformation beyond individual station precision from dense Global Navigation Satellite System (GNSS) networks in France and western, *Europe. Solid Earth,* **10,** 1905–1920.

Mazzotti, S., 2007. Geodynamic models for earthquake studies in intraplate North America, *Spec. Pap.-Geol. Soc. Am.,* **425,** 17–33.

Mazzotti, S., Jomard, H. & Masson, F., 2020. Processes and deformation rates generating seismicity in metropolitan France and conterminous Western Europe, *Bull. Soc. Géol. France,* **191**(1), 19, doi:10.1051/bsgf/2020019.

Mutschlecner, J.P. & Whitaker, R.W., 2005. Infrasound from earthquakes, *J. geophys. Res.,* **110,** doi:10.1029/2004JD005067.

Pearson, K., 1895. Notes on regression and inheritance in the case of two parents, *Proc. R. Soc. Lond.,* **58,** 240–242.

Pilger, C., Gaebler, P., Ceranna, L., Le Pichon, A., Vergoz, J., Perttu, A., Tailpied, D. & Taisne, B., 2019. Infrasound and seismoacoustic signatures of the 28 September 2018 Sulawesi super-shear earthquake, *Nat. Hazards Earth Syst. Sci.,* **19,** 2811–2825.

Preusse, P., Ern, M., Bechtold, P., Eckermann, S.D., Kalisch, S., Trinh, Q.T. & Riese, M., 2014. Characteristics of gravity waves resolved by ECMWF, *Atmos. Chem. Phys.,* **14,** 10 483–10 508.

Rivera, L. & Kanamori, H., 2014. Diagnosing source geometrical complexity of large earthquakes, *Pure appl. Geophys.,* **171,** 2819–2840.

Ritz, J.-F., Baize, S., Ferry, M., Larroque, C., Audin, L., Delouis, B. & Mathot, E., 2020. Surface rupture and shallow fault reactivation during the 2019 Mw 4.9 Le Teil earthquake, *France Commun. Earth. Environ.,* **1,** 10, doi:10.1038/s43247-020-0012-z.

RFS 2001-01., 2001. French Safety Rule, published by the French Nuclear Safety Authority, https://www.asn.fr/Reglementer/Regles-fondamentales-de-surete/RFS-relatives-aux-REP/RFS-2001-1-RFS-I.1.c.-du-31-05-2001.

Russell, D.R., 2006. Development of a time-domain, variable-period surface wave magnitude measurement procedure for application at regional and teleseismic distances. Part I—Theory, *Bull. seism. Soc. Am.,* **96,** 665–677.

Saikia, C., 1994. Modified frequency–wave number algorithm for regional seismo-grams using Filon's quadrature; modelling of Lg waves in eastern North America, *Geophys. J. Int.,* **118,** 142–158.

Sèbe, O., Guilbert, J. & Bard, P.-Y., 2018. Spectral factorization of the source time function of an earthquake from coda waves, application to the 2003 Rambervillers, France, earthquake, *Bull. seism. Soc. Am.,* **108**(5A), 2521–2542.

Segall, P. & Harris, R., 1987. Earthquake deformation cycle on the San Andreas fault near Parkfield, California, *J. geophys. Res.,* **92**(B10), 10 511–10 525.

Spearman, C., 1904. The proof and measurement of association between two things, *Am. J. Psychol.,* **15**(1), 72–101.

Szuberla, C.A.L. & Olson, J.V., 2004. Uncertainties associated with parameter estimation in atmospheric infrasound arrays, *J. acoust. Soc. Am.,* **115,** 253–258.

Vallage, A. & Bollinger, L., 2020. Testing fault models in intraplate settings: a potential for challenging the seismic hazard assessment inputs and hypothesis? *Pure appl. Geophys.,* **177,** 1879–1889.

Vanek, J., Zatopek, A., Karnik, V., kondorskaya, N.V., Riznichenko, Y.V., Savarensky, E.F., Solov'ev, S.L. & Shebalin, N.V., 1962. Standardization of magnitude scales, *Bull. Acad. Sci. USSR Geophys. Ser.,* 108–111.

Veinante-Delhaye, A. & Santoire, J.-P., 1980. Sismicité récente de l'Arc Sud-Armoricain et du Nord-Ouest du Massif Central. Mécanismes au foyer et tectonique, *Bull. Soc. Géol. France,* (7), t. XXII, N°1, p, 93–102.

Virieux, J., Garnier, N., Blanc, E. & Dessa, J.X., 2004. Paraxial ray tracing for atmospheric wave propagation, *Geophys. Res. Lett.,* **31,** doi:10.1029/2004GL020514.

Wagner, J. *et al.*, 2017. Observed versus simulated mountain waves over Scandinavia – improvement of vertical winds, energy and momentum fluxes by enhanced model resolution? *Atmos. Chem. Phys.,* **17,** 4031–4052.

Walker, K.T., Pichon, A.L., Kim, T.S., de Groot-Hedlin, C., Che, I.-Y. & Garcés, M., 2013. An analysis of ground shaking and transmission loss from infrasound generated by the 2011 Tohoku earthquake, *J. geophys. Res.,* **118**(23), 12 831–12 851.

SUPPORTING INFORMATION

Supplementary data are available at *GJI* online.

Figure S1. Zoom on Figure 2.(b) in order to allow the reader to better see all the details of the geological cross-section with the Valvignères borehole superimposed.

Figure S2. LDG 1-D velocity model used for seismic event locations and moment tensor analysis at the CEA.

Figure S3. Jackknife test solutions showing the stability of the moment tensor inversion in terms of focal mechanisms, moment magnitude (Mw) and variance reduction (VR) when 9 (left-hand panel), 8 (middle panel) and 7 (right-hand panel) stations out of 10 are used. The solution obtained using the entire pool of data (10 stations) is shown in red. The horizontal axes show the number of combinations used for each case.

Figure S4. Moment tensor grid search applied to the Le Teil earthquake. The yellow star shows the revised location. The red triangles show the CEA stations while the RESIF stations are shown by the blue triangles. The beachballs obtained at each point of the grid are colour-coded (and sized) by the variance reduction (VR). The point sources are spaced every 0.2° in latitude and longitude and forced at 1 km depth, except within a radius of about 96 km centred on the source where the spacing is 0.1° in latitude and longitude. The best solution of the grid search is found at 0.1° from the source location, with a comparable source mechanism (top right-hand side) that the one obtained at the epicentre (top left-hand side).

Figure S5. Map of the 48 broad-band seismic stations (triangles) used for the calculation of the surface wave magnitude (MS) of the Le Teil event (red star). The colour of the triangles indicates the MS values measured at each station.

Figure S6. Selected surface wave records of Le Teil event observed between 22° and 90°. The traces are ordered by epicentral distances. The MS value corresponding to each of them is given. The green area indicates the time period during which, the maximum amplitude is determined. It is based on the 3-D velocity model of Ritzwoller and Shapiro (2002). SNR means signal-to-noise ratio.

Figure S7. Sentinel-1 wrapped coseismic interferograms with different look directions. The black dashed line represents the inverted fault surface trace.

Figure S8. Downsampled unwrapped interferograms with different look direction, (middle line) synthetics for the best-fitting single-fault model, and (bottom line) residuals between data and model. Black box represents the surface projection of the inverted fault geometry.

Figure S9. RMS misfit plot for various fault dip angle models. The red circle shows the best fit dip model shown in the Figs 4 and S6.

Figure S10. (a) Vertical displacement amplitude with the horizontal displacement arrows. (b) Absolute displacement (b), compared to the peak surface pressure (PSP) map (c) already shown in Fig. 4(d).

Figure S11. Parabolic equation (PE) simulations at 1 Hz to derive the attenuation of the acoustic energy at OHP, ∼110 km away from Le Teil (taken at reference of 1 km from the source). (a, d) Vertical

profile of the effective sound speed (black solid line) with (a) and without (d) the perturbation by one gravity wave realization (red solid line) of the (modified) Gardner *et al.* (1993)'s model with perturbation amplitudes multiplied by two (see text S4 for details). The vertical dashed line marks the sound speed at the surface. (b, e) Attenuation of the acoustic energy as a function of the distance to Le Teil corresponding to the meteorology (a) and (d), respectively. Light grey lines represent the predicted attenuation from the ground level to a level of 2 km, with the dark grey lines indicating the maximum amplitude. (c, f) Acoustic energy attenuation through the atmosphere with ray paths superimposed (grey lines). The attenuation is colour coded (in dB) and the OHP station indicated (green triangle).

Figure S12. Modelled infrasound waveforms using normal modes (bottom) with gravity wave perturbations (13 realizations, see text S4) added to the ECMWF wind and temperature profiles. Synthetic signals are compared to that of the observed one (blue box at the top). The x-axis indicates the corresponding celerity values and the y-axis the absolute (top) and normalized (bottom) amplitudes.

Figure S13. H/V ratios measured over metropolitan France for Le Teil earthquake. (a) Map of H/V ratio per station. Colour is proportional to H/V. (b) H/V ratios as a function of epicentral distance in log-log scale. H/V is estimated considering the mean PGA over the 2 horizontal components for all 3-component stations. The mean of H/V ratios is 1.49 (dashed blue line), which is extremely close to 3/2. H/V ratios follow a lognormal distribution (histogram and red curve). The normal distribution fit of the logarithm in base 10 of the data gives $\mu = 0.15$ (dashed red line) and $\sigma = 0.15$ (dotted red lines).

Table S1. Uncertainties in the focal mechanism and magnitude estimation of the Le Teil earthquake following the Jackknife test. The optimal solution using 10 regional stations is shown in Figure 3.

Table S2. Description of the Sentinel-1 interferograms used in this study.

Table S3. Domains of validity in magnitude and in distance indicated by the authors for the four GMPEs presented in Fig. 4. BT03: Berge-Thierry *et al.* (2003), Ma04: Marin *et al.* (2004), DC15: Drouet & Cotton (2015) and Am17: Ameri *et al.* (2017). M_s, surface magnitude; M_L, local magnitude; M_w, moment magnitude. R_{hypo}, hypocentral distance; R_{epi}, epicentral distance.

Please note: Oxford University Press are not responsible for the content or functionality of any supporting materials supplied by the authors. Any queries (other than missing material) should be directed to the corresponding author for the paper.